

Low-Energy Magnetic Excitations and Morphology in Layered Hybrid Perovskite–Poly(dimethylsiloxane) Nanocomposites

Alexandros Lappas,^{*,†} Andrej Zorko,[‡] Etienne Wortham,[†] Rabindra N. Das,[§]
Emmanuel P. Giannelis,[§] Pavel Cevc,[‡] and Denis Arčon^{‡,||}

Institute of Electronic Structure & Laser, Foundation for Research & Technology—Hellas, Vassilika Vouton, 71110 Heraklion, Greece, Institute “Jožef Stefan”, Jamova 39, 1000 Ljubljana, Slovenia, Department of Materials Science and Engineering, Cornell University, Ithaca, New York 14853, and Faculty of Mathematics and Physics, University of Ljubljana, Jadranska 19, 1000 Ljubljana, Slovenia

Received July 30, 2004. Revised Manuscript Received December 3, 2004

Hybrid organic–inorganic layered perovskites $(R_n\text{NH}_3)_2\text{MnCl}_4$ of lyophilic aliphatic cations $R_n\text{NH}_3^+$ ($R_n = \text{C}_n\text{H}_{2n+1}$; $n = 2, 9$) have been studied for their potential as functional additives in poly(dimethylsiloxane) (PDMS). The evolution of the microstructure for various nanocomposite assemblies was characterized by means of X-ray diffraction and electron microscopy. Composites consisted of exfoliated MnCl_4 layers and enhanced aspect ratio crystallites composed of bundles of a few MnCl_4 sheets have been prepared. Such local morphology characteristics give rise to an inhomogeneous microstructure with enhanced surface areas and pronounced structural defects, suggestive of partial polymer intercalation only for the longer chain systems. The degree to which the two chemical realms interact at the interfacial regions does not affect the static magnetic properties. The composites display two-dimensional Heisenberg antiferromagnetic behavior ($T_N \leq 42$ K) similar to that in bulk powders. Electron paramagnetic resonance finds that the low-temperature spin dynamics of dispersed MnCl_4 layers are determined by the magnons and static solitons as in bulk materials. On the other hand, size-dependent features and local scale imperfections in the morphology, arising from the composite formation, soften the low-energy magnetic excitations of the pinned solitons. The interaction of PDMS and organocation chains affects the dynamics and the orientational ordering of the longer, linear alkylammonium molecules.

Introduction

Composite organic–inorganic materials are formed when at least two distinctly dissimilar materials are mixed on a nanometer length scale to obtain unique characteristics by acquiring synergy between the two chemical species.¹ More specifically, interactions between inorganic layered materials and organic substances have attracted increasing interest especially in view of unique host–guest interactions and their potential in a range of scientific and industrial applications.² It has been shown that syntheses of such hybrids³ either by direct intercalation of polymers into inorganic hosts or by pre-intercalation of their monomers and in situ polymerization opens new routes to construct novel inorganic–polymer nanoassemblies.⁴ Although a large number of inorganic compounds exhibit intercalation⁵ capabilities layered silicates

are ideal representatives in this field, with a plethora of interactions forming new clay–polymer composites.⁶ The compositional and structural variations generated by introducing a few weight percent of clay into the polymer matrix give rise to nanocomposite materials exhibiting unique interfacial properties that enhance chemical resistance, mechanical strength, thermal stability, and optical transparency.⁷

Motivated by the extraordinary performance of layered silicates in nanocomposite design, we search for other lamellar inorganic solids that by dispersion in an appropriate organic matrix can display similar multifunctional qualities in the nanometer length scale. We found a good candidate among layered organic–inorganic perovskites,⁸ of the general formula $(\text{C}_n\text{H}_{2n+1}\text{NH}_3)_2\text{MX}_4$ — $\text{M} = \text{metal (Mn)}$, $\text{X} = \text{halogen (Cl)}$, $n \geq 1$ —which are prototype models for two-dimensional (2D) classical spin antiferromagnets.^{9,10} By

* Corresponding author: (e-mail) lappas@iesl.forth.gr.

† Foundation for Research & Technology—Hellas.

‡ Institute “Jožef Stefan”.

§ Cornell University.

|| University of Ljubljana.

- (1) Gomez-Romero, P. *Adv. Mater.* **2001**, *13*, 163. Mitzi, D. B. *J. Chem. Soc., Dalton Trans.* **2001**, 1. Sanchez, C.; Ribot, F.; Lebeau, B. *J. Mater. Chem.* **1999**, *9*, 35.
- (2) Pinnavaia, T. J. *Science* **1983**, *220*, 365.
- (3) Currey, J. D. *J. Mater. Educ.* **1987**, *9*, 119.
- (4) Ziolo, R. F.; Giannelis, E. P.; Weinstein, B. A.; O'Horo, M. P.; Ganguly, B. N.; Mehrotra, V.; Russell, M. W.; Huffman, D. R. *Science* **1992**, *257*, 219.
- (5) Bruce, D. W.; O'Hare, D. *Inorganic Materials*, 2nd ed.; John-Wiley & Sons Ltd.: New York, 1996.

- (6) Usuki, A.; Kawasumi, M.; Kojima, Y.; Okada, A.; Kurauchi, T.; Kamigaito, O. *J. Mater. Res.* **1993**, *8*, 1174. Usuki, A.; Kojima, Y.; Kawasumi, M.; Okada, A.; Fukushima, Y.; Kurauchi, T.; Kamigaito, O. *J. Mater. Res.* **1993**, *8*, 1180.
- (7) Messersmith, P. B.; Stupp, S. I. *J. Mater. Res.* **1992**, *7*, 2599. Okada, A.; Usuki, A. *Mater. Sci. Eng.* **1995**, *C3*, 109. Giannelis, E. P. *Adv. Mater.* **1996**, *8*, 29. Wang, Z.; Lan, T.; Pinnavaia, T. J. *Chem. Mater.* **1996**, *8*, 2200.
- (8) Mitzi, D. B. In *Progress in Inorganic Chemistry*; Karling, K. D., Ed.; Wiley: New York, 1999; Vol. 48.
- (9) Achiwa, N.; Matsuyama, T.; Yoshinari, T. *Phase Transitions* **1990**, *28*, 79.
- (10) Flandrois, S.; Chanh, N. B.; Duplessix, R.; Maris, Th.; Negrier, P. *Phys. Status Solidi A* **1995**, *149*, 697.

varying n , the separation between layers can be tuned so that interactions between perovskitic layers can become sufficiently weak avoiding the intrinsic interlayer coupling present in the bulk two-dimensional compounds. Fundamental magnetic properties of the 2D square-lattice of classical spins can then be studied experimentally and compared to existing theoretical models. Irrespective of n , interlayer interactions cannot be completely ignored and alternative approaches are needed to explore true 2D systems. In view of that we wanted to test the possibility of the perovskite exfoliation in a polymer matrix, stability of exfoliated nanoparticles and the impact of delamination on the magnetic properties of these particles. Our optimism laid on the fact that the perovskite intragallery $R_n\text{NH}_3^+$ ($R_n = \text{C}_n\text{H}_{2n+1}$) cation is potentially capable of functioning as a compatibilizing agent (i.e., organophilic) between the inorganic layers and the polymer matrix by analogy to what is known for the protonated amines of clays.¹¹ It is especially desirable to attain classes of materials based on delaminated sheets as in the general case the resultant homogeneous mixture of polymer–inorganic layers may give rise to new physical properties that are not accomplished by one of the two species alone. Therefore the question of interest is how the MnCl_4 -based lamellae would function chemically inside the polymer matrix, whereas focus on the physical properties would allow monitoring the electronic functionality of the MnCl_4 -layers. We stress that this approach could be extended to other quasi-2D systems and that it is not limited to the particular chemical system we have chosen.

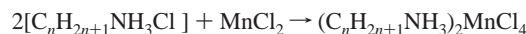
With this work we report the preparation of composite samples made of dispersed perovskitic MnCl_4^{2-} layers in a poly(dimethylsiloxane) (PDMS) matrix and the influence of the nanocomposite formation $\{(\text{C}_n\text{H}_{2n+1}\text{NH}_3)_2\text{MnCl}_4\text{-PDMS}\}$ ($n = 2, 9$) on the magnetic properties. When the same solvent-based processing method was employed for matrixes based on other polymers, such as poly(methyl methacrylate) or poly(ethyl methacrylate), relatively less uniform samples were obtained, making PDMS the choice of preference. The morphology of the PDMS-based multicomponent systems was first characterized by using a combination of X-ray diffraction (XRD) and conventional transmission electron microscopy (TEM). We found that as-prepared composites consist of either exfoliated MnCl_4 layers or enhanced aspect ratio crystallites, composed of bundles of a few MnCl_4 sheets, while exploring their size dependency on n . The composites still show a transition to a three-dimensional (3D) ordered Néel state, while it seems that the transition temperature ($T_N \sim 42$ K) is not strongly affected by the nanoparticle morphology. The electron paramagnetic resonance (EPR) measurements in bulk $(\text{R}_n\text{NH}_3)_2\text{MnCl}_4$ powder samples demonstrate that, at low temperatures, nonlinear magnetic excitations or spin solitons determine the dynamical spin correlation function as probed by the line width of the EPR signal in the vicinity of the magnetic transition. Such a two-dimensional behavior is also apparent when systems of dispersed MnCl_4 layers are measured for various composites.

In addition, EPR studies revealed that the soliton energy is systematically smaller in composite samples compared to bulk powders, which can be interpreted in terms of the increase of concentration of structural imperfections, such as stacking faults, for example. These centers are most probably generated during the exfoliation process.

Experimental Methods

Hybrid Perovskite Syntheses. Various alkylammonium chloride salt powders, $\text{C}_n\text{H}_{2n+1}\text{NH}_3\text{Cl}$ ($n = 2, 9$) were synthesized according to standard solid-state chemistry procedures involving anaerobic conditions. The neutral amines were dissolved in distilled water with a slight excess of concentrated HCl in a three-neck flask under inert (N_2) gas flow and constant stirring. After 1–2 h the solutions were heated at 60 °C to promote evaporation of water, and then the powders were removed from the flask and dried under dynamic vacuum (10^{-2} mbar) inside a desiccator (for $n = 2, 9$). Hereafter, ethyl- ($n = 2$) and nonyl- ($n = 9$) ammonium when used will be abbreviated to EA and NOA, respectively.

Parent perovskites were synthesized as reported previously.¹² In a dry controlled-atmosphere (Ar) glovebox, high-purity MnCl_2 and alkylammonium chloride salt powders were intimately mixed with the molar ratio 1:2. The mixtures were sealed in Pyrex tubes under argon partial pressure ($P \cong 300$ mTorr) and heated for 5 days at 150 °C. At the second stage, the powders were taken back in the glovebox where they were reground and reacted at 200–220 °C in sealed ampules, filled with ~ 300 mTorr of Ar, for two additional days to facilitate the reaction:



After the second treatment at elevated temperatures, the samples were not sensitive to ambient atmosphere conditions ($\text{O}_2/\text{H}_2\text{O}$) anymore.

Polymer Nanocomposite Fabrication. In the present investigation, we have used PDMS as the matrix to disperse the perovskite, although polymers such as the poly(methyl methacrylate) or poly(ethyl methacrylate) were also employed but less successfully. Optimum viscosity for the PDMS not only favors the current composite processing technology but also helps to avoid precipitation, segregation, and phase separation of the perovskite components in the polymer matrix. Relatively more uniform nanocomposites were then attained as favorable viscosity, minimum shrinkage and fast curing, properties difficult to achieve with the other polymers, made our PDMS-based systems more homogeneous under speed mixing.

The raw materials that were required for the preparation of polymer nanocomposite were PDMS ($M_w = 64\,000$; PS 445, United Chemical Technologies), trimethylsilyl-terminated poly(dimethyl-co-hydromethyl)siloxane copolymer (cross-linking agent; HMS-301, Gelest, Inc.), Pt–divinyltetraethylsiloxane complex (SIP 6830.0, Gelest, Inc.), and Mn–perovskite (cf. nanofillers). To investigate the effect of particle/filler dispersion, a series of the organically modified perovskite–PDMS-based nanocomposites were prepared. In a typical procedure, the parent Mn–perovskite powders were mixed with tetrahydrofuran (THF) solution (10 wt %) to form slurry. The slurry was stirred for 12 h and then ultrasonicated for 25 min to minimize particle agglomeration and avoid the segregation of the insoluble Mn complex. $\{(\text{C}_n\text{H}_{2n+1}\text{NH}_3)_2\text{MnCl}_4\text{-PDMS}\}$ nanocomposites were prepared by speed mixing the appropriate amount of MnCl_4 complex/THF slurry with vinyl-terminated PDMS and

(11) Wang, Z.; Massam, J.; Pinnavaia, T. J. In *Polymer-Clay Nanocomposites*; Pinnavaia, T. J., Beall, G. W., Eds.; John-Wiley & Sons Ltd.: Chichester, 2000; pp 127–149.

(12) Wortham, E.; Zorko, A.; Arcon, D.; Lappas, A. *Physica B* **2002**, *318*, 387.

trimethylsilyl-terminated poly(dimethyl-*co*-hydromethyl)siloxane copolymer (MeHSiO) (reactivity ratio, $r = 2$) at 3000 rpm for 5–7 min. THF solubilizes PDMS, reduces the viscosity of the polymer, and improves the polymer–filler (Mn complex) interactions. After complete evaporation of THF, a stoichiometric amount of platinum–divinyltetramethyldisiloxane (MeHSiO:Pt = 50:1) catalyst was added to the mixture and speed mixed for an additional 30 s. The resulting material was allowed to cure at room temperature for a minimum 2 h. In the present work we synthesized composites with only 3.5(1)% weight $(R_n\text{NH}_3)_2\text{MnCl}_4$ ($n = 2, 9$) in PDMS. Although lower weight perovskite dispersions could be realized, they were too dilute thus making difficult the characterization of the hybrid system's morphology. On the other hand higher density perovskite composites were avoided, as phase-separated mixtures were easily achieved.

Materials Characterization. To monitor the formation and structure variation in these materials XRD analyses was carried out with a Rigaku D/MAX-2000H rotating anode diffractometer (Cu K α radiation) equipped with secondary pyrolytic graphite monochromator. Room-temperature powder patterns were collected for the polycrystalline $(R_n\text{NH}_3)_2\text{MnCl}_4$ ($n = 2, 9$) compounds. In the case of the perovskite–PDMS composites, the specimens were cut out from the bulk material in the form of a thick ribbon. The quantitative analysis of the diffraction data, involving complete profile fitting by the LeBail pattern decomposition method,¹³ was carried out with the FULLPROF¹⁴ suite of programs.

Ultrathin slices (70 nm thick) of the samples were prepared by cutting them out from the bulk perovskite–PDMS composite materials utilizing cryogenic (–150 °C) microtoming. TEM investigations were performed with a JEOL 1200EX (120 keV). TEM photographs were taken with the scattering contrast in the bright-field mode, up to 100 000 magnification to assign the relative contributions of the nanoscopic aspects of the hybrids to their macroscopic response. In this way darker lattice fringes would correspond to periodic stacking of the (heavier element) perovskite layers, whereas the organic matrix would be represented by the variable shading (due to local density fluctuations) surrounding.

The static magnetic properties of the materials were investigated by dc susceptibility measurements on a Quantum Design MPMS superconducting quantum interference device (SQUID) magnetometer. Data were obtained under zero-field cooled (ZFC) and field cooled (FC) protocols, between 4.5 and 300 K, for both bulk powdered organic–inorganic (O–I) perovskite samples and their polymer composites. Measurements were carried in applied fields of either 0.5 kG for the powder samples or 1 kG for the composites. The modification of the ground-state magnetic properties, especially for the filled polymer containing inorganic layers and the associated spin dynamics, were further studied by the EPR technique. X-band EPR spectra were collected on a commercially available Bruker E580 FT/CW spectrometer working at Larmor frequency of $\nu_1 \approx 9.5$ GHz, equipped with an Oxford Cryogenics cryostat. The temperature stability was better than ± 0.1 K. In all samples studied by EPR we used the same cooling protocol: slow cooling from room temperature to ~ 60 K taking a spectrum every 5 K. After that the temperature step was decreased to 1 K, while in the vicinity of magnetic transition data were taken every 0.5 K.

Results and Discussion

Structure of O–I Perovskites. In view of the developments of polymer composites containing inorganic fillers

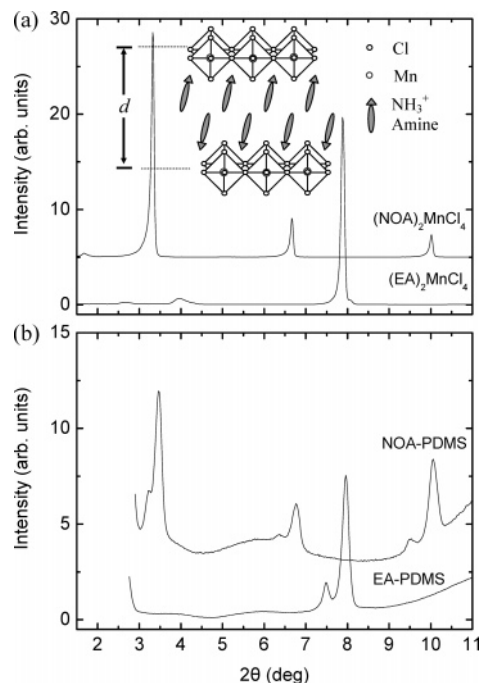


Figure 1. X-ray diffraction patterns showing Bragg scattering from the (00*l*) basal reflections of the perovskitic layers from (a) the bulk powder $(C_nH_{2n+1}NH_3)_2MnCl_4$ samples ($n = 2, 9$) (inset: graphical representation of the $(C_nH_{2n+1}NH_3)_2MnCl_4$ two-dimensional structure) and (b) the hybrid $\{(C_nH_{2n+1}NH_3)_2MnCl_4\text{-PDMS}\}$ material specimen, in the form of thin rectangular slice cut out from the as-made composites.

(silicates) one can envisage the role of perovskite to be analogous to that of clay nanoparticle additives in polymer layered silicate nanocomposites. To rationalize the necessity for the chemical syntheses described previously and to probe modifications in the physical behavior between parent and composite systems, let us introduce some special structural features justifying the selection the O–I perovskites as the active motifs for new functional (nano)assemblies. Figure 1a shows the XRD powder patterns for every one of the $(C_nH_{2n+1}NH_3)_2MnCl_4$ ($n = 2, 9$) O–I perovskites. LeBail pattern decomposition of these data supports the orthorhombic symmetry of their crystal lattice and allows indexing of the Bragg peaks upon the $Cmca$ space group in agreement with earlier reports.¹⁵ The strong layering nature of these systems is exemplified by the observation of intense, sharp (00*l*) ($l = 2n$; $n = \text{integer}$) reflections, which are characteristically shifted toward lower angles with progressive increase of the organocation chain length. This confirms the enhanced interlayer separation, $d (= c/2)$, of the $MnCl_4$ sheets upon the intercalation of longer chain alkylammonium $C_nH_{2n+1}NH_3^+$ groups. The present results, in agreement with earlier reports,¹⁰ show that the separation d between layers is varied almost linearly upon increasing n values. This effect served as incentive for choosing these materials as candidate “loading agents” for novel polymer nanocomposites in analogy to the plethora of organophilic clay applications. The ability of hybrid perovskites to self-assemble⁸ into nanostructures of multilayered inorganic sheets interleaved by bilayers of organic cations (inset Figure 1a), while possessing weak van der Waals interactions between their organic tails,

(13) LeBail, A.; Duroy, H.; Fourquet, J. L. *Mater. Res. Bull.* **1988**, *23*, 447.

(14) Rodríguez-Carvajal, J. *Physica B* **1993**, *192*, 55.

(15) Depmeier, W.; Felsche, J.; Wildermuth, G. *J. Solid State Chem.* **1977**, *21*, 57. Depmeier, W. *J. Solid State Chem.* **1979**, *29*, 15.

Table 1. Evolution of the Interlayer Spacing, d , and Particle Size Characteristics^a upon Increasing Alkylammonium Chain Lengths, $C_nH_{2n+1}NH_3^+$ ($n = 2, 9$), As Determined from the XRD (002) Basal Reflections

compound	bulk parent perovskite				polymer nanocomposite							
	primary ^b				primary ^b				secondary ^b			
	$d/\text{\AA}$	b/rad $\times 10^{-3}$	$L_c/\text{\AA}$	no. of layers	$d_1/\text{\AA}$	b_1/rad $\times 10^{-3}$	$L_{c1}/\text{\AA}$	no. of layers	$d_2/\text{\AA}$	b_2/rad $\times 10^{-3}$	$L_{c2}/\text{\AA}$	no. of layers
(EA) ₂ MnCl ₄	11.024	1.66	838	76	11.107	2.95	471	42	11.806	2.90	480	41
(NOA) ₂ MnCl ₄	26.566	1.24	1119	42	25.927	3.05	454	18	27.988	5.32	260	9

^aIncluding peak broadening, b , average crystallite size, L_c , and number of coherently stack layers. ^b(002) reflections.

as compared to the stronger hydrogen bonding of the NH_3^+ to the inorganic sheets, makes them good candidates to undergo exfoliation processes when they become dispersed in the favorable, lyophilic environment of a polymer-based matrix.

Structure and Morphology of Composites. To understand the electronic and magnetic properties of the dispersed inorganic filler particles we studied their assembly and average size within the polymer matrix by means of combined TEM and XRD studies. The evolution of the composite system's morphology upon the $(R_nNH_3)_2MnCl_4$ ($n = 2, 9$) perovskite incorporation demonstrates the influence of the alkylammonium chain length in the microstructure.

A preliminary inspection of the XRD patterns (Figure 1b) of the as-prepared perovskite–polymer composites, reveals “secondary” peaks at Bragg angles (d_2) systematically lower than the angles (d_1) corresponding to the “primary” (00 l) basal reflections of the parent perovskites (Figure 1a). These secondary peaks are found, for example, at $2\theta_2 = 7.48^\circ$ for the $\{(EA)_2MnCl_4\text{--}PDMS\}$ nanocomposite material and at $2\theta_2 = 3.18^\circ, 6.32^\circ$ and 9.44° for the $\{(NOA)_2MnCl_4\text{--}PDMS\}$. The secondary reflections in all cases were indexed on the basis of the same orthorhombic lattice symmetry ($Cmca$) as to that adopted by the parent perovskites. In principle their lower angle shift would suggest an expanded c -axis unit cell and a moderate increase in the interlayer d -spacing (d_2). The extent to which the perovskite lamellar structure is primed apart, during the polymer composite formation, for various length $C_nH_{2n+1}NH_3^+$ groups is compiled in Table 1. We note a marginal change in the case of the EA composites, with however, a more pronounced layer “opening” ($>2 \text{\AA}$) in the NOA composite samples. As a number of factors,¹⁶ unrelated to the intrinsic chemical/physical functionality of the filler particles (e.g., sample geometry, smoothness of sample surface, perovskite concentration, etc.), may also affect the Bragg peak positions and their intensities in the experimentally observed XRD patterns, TEM is necessary to determine more aspects of the microstructure in such hybrid materials.

a. Transmission Electron Microscopy. The TEM experiments resolve regions of different layer spacing, while allow us to discuss the arrangement of individual layers, stacks of layers inside the composites, or both. For $\{(NOA)_2MnCl_4\text{--}PDMS\}$ nanocomposite material, bright-field TEM micrographs show bundles of layers of the $(NOA)_2MnCl_4$ perovskite particles at $l \sim 300\text{--}400 \text{ nm}$ apart (Figure 2a). This

effect is less pronounced for the short-chain $(EA)_2MnCl_4$ -based hybrid material (Figure 2b). Near the primary $(NOA)_2MnCl_4$ particle–polymer interface there is significant disruption of original crystallite structure, with the PDMS penetrating the interior of the particle, giving rise to both *small* (inset Figure 2a; “region 1”) openings near the edge and *larger* gaps (inset Figure 2a; “region 2”) between layer stacks. At the same time the interior of the crystallites shows “local fluctuations” in the layer stacking, indicating the presence of defect structures (e.g., stacking faults; inset Figure 2a, “region 3”). These *inhomogeneities* can be a source of disagreement between the interlamellar space magnitude estimated by the *average* structure determined by XRD and the *local* structure resolved by TEM observations.

Figure 2b presents the case of $\{(EA)_2MnCl_4\text{--}PDMS\}$ where the original crystallite structure shows relatively higher layer disorder, without coherent stacks of layers in proximity ($l > 400 \text{ nm}$) and with smaller “longitudinal” dimensions when compared to that in $\{(NOA)_2MnCl_4\text{--}PDMS\}$. The disordered layer groupings of $\{(EA)_2MnCl_4\text{--}PDMS\}$ appear to maintain their gallery heights while layer delamination is more pronounced at the interfacial regions of the $(EA)_2MnCl_4$ crystallites. Therefore, individual layers together with small stacks of $MnCl_4^{2-}$ sheets, of longitudinal dimensions 50–150 nm, randomly distributed within the polymer, result in a heterogeneous microstructure for the EA-containing samples. On the other case, bundles of $MnCl_4^{2-}$ sheets composed of enhanced aspect ratio $(NOA)_2MnCl_4$ crystallites (namely, 200–400 nm longitudinal dimensions) that orient themselves with one another allow for a highly anisotropic ordered microstructure (Figure 2a). The larger area TEM images for the NOA-containing materials also demonstrate the mechanical flexibility of the “filler” perovskitic inorganic layers, as they bend smoothly while forming their stacks in individual crystallites (Figure 2a).

In summary, TEM finds that although intercalation by PDMS in the interior of the $MnCl_4$ -based layer stacks is not afforded in a uniform way, moderate flocculation and separation of the original crystallites by the surrounding organic matrix does take place near the boundary of the primary particle–polymer interface.

b. X-ray Diffraction Considerations. As seen by TEM and witnessed by the double-peak structure of the XRD probe (Figure 1b), mainly the modulation of the interlayer spacing at the particle–polymer interfacial regions should be responsible for the apparent increase of the interlayer space. Combining the information from the average structure probed by XRD work with microscopic TEM observations, we

(16) Vaia, R. H.; Liu, W. *J. Polym. Sci. Part B: Polym. Phys.* **2002**, *40*, 1590.

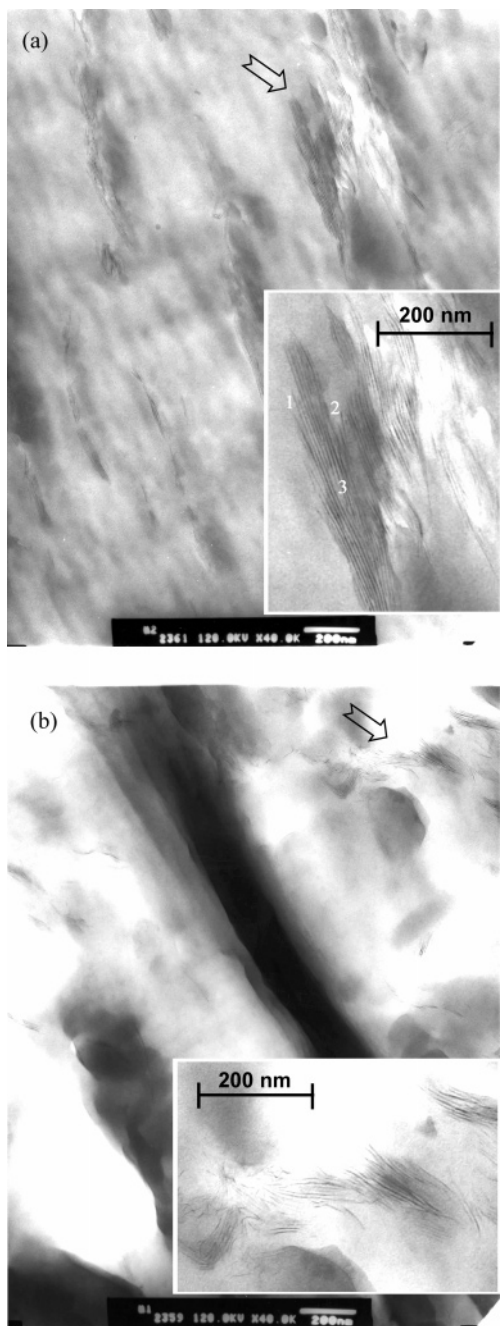


Figure 2. Larger area bright-field TEM image of composite specimens: (a) $\{(NOA)_2MnCl_4\}$ -PDMS and (b) $\{(EA)_2MnCl_4\}$ -PDMS. The former displays layer groupings with mutual crystallite ordering in the interparticle regions of the PDMS matrix. The arrows indicate the areas of the composite shown in magnification as insets: (a) primary particle with small and large crystallite openings {1, 2}, layer intergrowths and stacking faults {3}; (b) a region of composite showing randomly distributed crystallites and individual perovskitic layers.

postulate (vide infra) that these hybrid composite materials display a *heterogeneous* (in terms of size, arrangement, and stacking of layers) local-scale morphology, assigned to (i) *intercalated* regions, contributions from near the boundaries of the crystallites with the polymer (“secondary” XRD reflections, define d_2) and (ii) *unintercalated* regions at the interior of the particles themselves (“primary” XRD reflections, define d_1). Table 1 compares the relative changes in the d -spacing of the $MnCl_4$ -sheets in powders and composites as derived from the XRD studies.

Quantitative analysis of the XRD intensity profile complements the TEM analysis as it allows characterizing to some extent the *layer-to-layer correlations* inside the nanocomposite. The degree of layer stacking (forming perovskite particles dispersed in the polymer matrix), addressing particle size, internal disorder effects, or both, can be evaluated by the *broadening* and *weakening* of the intensity for the primary and secondary basal reflections (Figure 1b). As the width of the peaks is inversely proportional to the coherence length of the scattering entities, a *lower bound* for the *coherent stacking* (along c -axis) of the perovskitic layers can be estimated. This is approximated by calculating the average crystallite size through the Scherrer formula, $L_z = (0.9\lambda)/(b \cos\theta)$, where b is full width at half-maximum (fwhm) in radians (Table 1). Although in the bulk powdered perovskites, the average fwhm of the primary (002) XRD peaks displays some reduction upon increasing alkylammonium chain length, when the $(C_nH_{2n+1}NH_3)_2MnCl_4$ ($n = 2, 9$) are dispersed in the PDMS, importantly, we find the primary (00 l) peaks to become at least $\sim 50\%$ broader. Furthermore, the secondary peaks, in the composites, which have “grown” due to partial polymer inclusion in the interlayer space of the perovskite, appear to have developed broader with the increase in the number of carbon atoms in the $C_nH_{2n+1}NH_3^+$ groups.

Such broadening effects, determined by the length of the coherent X-ray scattering *perpendicular* to the layers, suggest that the length over which coherency exists for crystallites formed in the composites must decrease. As a matter of fact if we estimate, from the primary reflections, the number of $MnCl_4^{2-}$ sheets stack together to form the dispersed particles we find that there is a radical diminution of the number of layers (Table 1). The crystallite *size reduction* is further pronounced when polymer inclusion is feasible, as the 2θ shift of (00 l) secondary peaks to lower angles gives rise to a larger $[b \cos\theta]$ term and therefore a smaller L_z . This is true for the longer chain $(NOA)_2MnCl_4$ -containing composites, but not for the short-chain $\{(EA)_2MnCl_4\}$ -PDMS system. For the former we estimate a *heterogeneous* particle size, ranging from 45 nm (110 nm in *bulk* powder) associated with unintercalated to 26 nm in the partially intercalated crystallites.

Rationalizing the causes that possibly produce deviations between the XRD and TEM extracted length scales, for the coherent layer-to-layer correlations (represented by the number of parallel stacked $MnCl_4$ layers and their interlamellar separation) in these hybrids, someone may claim contributions that either were not accounted for in the previous calculations or because structural features were difficult to resolve through the employed experimental tools. The origin of the former, for example, can be strain associated with the crystallite interfacial regions, that is likely to broaden further the XRD peaks and the latter may be related to the presence of defect structures that may introduce uncertainty in the interlayer spacing and therefore “misinterpret” the spatial extent of their stacking. The weak Bragg scattering received from such complex polymer hybrids limits the usage of methodologies based upon full profile (Rietveld) analysis that otherwise help clarifying such issues.

Magnetic Response of Composites. In a model system approach, the simplest two-dimensional (2D) magnet would consist of a quadratic arrangement of spins coupled by the isotropic Heisenberg exchange interaction $H_E = -\vec{J}_i \cdot \vec{S}_j$. A fairly good approximation for such a 2D antiferromagnetic Heisenberg square lattice is the present family of metal–organic compounds $(R_n\text{NH}_3)_2\text{MnCl}_4$.¹⁷ Here the Mn^{2+} ions are arranged in quadratic layers, octahedrally coordinated by Cl ions (inset Figure 1a), while double sheets of *organophilic* alkylammonium groups $\text{C}_n\text{H}_{2n+1}\text{NH}_3^+$ separate the MnCl_6 inorganic layers. By varying n , the separation between layers can be tuned. Intuitively, weak exchange interaction between the layers should scale with n while leaving the superexchange interactions within the individual Mn^{2+} sheets essentially unchanged. However, in an ideal 2D magnet no magnetic ordering at finite transition temperature is theoretically allowed.¹⁸ To attain a nonzero transition temperature one needs to introduce either interlayer exchange interactions or some other type of magnetic anisotropy, including Ising or Dzyaloshinsky–Moriya interaction.

In the section Structure and Morphology of Composites, it was demonstrated that when these systems are dispersed in the favorable *lyophilic* PDMS environment, the subsequent polymer nanocomposite formation affects the morphology of the perovskitic particles and results in smaller crystallite dimensions or even exfoliated layers. During such a process one expects that a relative proportion of the surface spins will increase compared to bulk powder. The enhanced specific surface and finite size effects are thus expected to play an important role in dispersed samples. Furthermore, as revealed by the TEM and XRD data, there are numerous defects formed during the exfoliation process, which may influence the spin dynamics and the magnetic ordering of the nanoparticles. On the other hand the interaction between the PDMS and organocation chains is envisaged to affect the dynamics and orientational ordering of the alkylammonium molecules. To this extent, it is especially interesting to probe existing or enhanced magnetic anisotropies due to the modified crystallite topology in such composites. In the following paragraphs we therefore examine the impact that size-dependent correlations can have on the magnetic properties of such nanoscale hybrids.

a. Bulk Magnetic Properties. In Figure 3 we compare the field-cooled dc magnetic susceptibility, $\chi(T)$ for all the $(\text{C}_n\text{H}_{2n+1}\text{NH}_3)_2\text{MnCl}_4$ ($n = 2, 9$) materials dispersed in the PDMS to those in bulk powder form. While there is no substantial change in the characteristic Néel ordering temperature, T_N , the magnitude of the magnetic moment in the pristine bulk samples^{10,12} is by a factor of ~ 2 larger than the corresponding moment size in dispersed samples. We note that such a reduction in the magnetic moment has been observed before in different nanostructured magnetic materials.¹⁹ A plausible explanation assumes that (due to the enhanced surface area, in addition to defects presented by

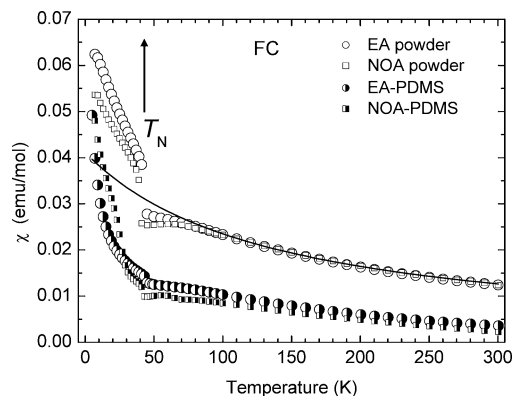


Figure 3. Temperature evolution of the dc spin susceptibility, χ , measured in a SQUID magnetometer for powder and polymer composites of $(\text{C}_n\text{H}_{2n+1}\text{NH}_3)_2\text{MnCl}_4$ ($n = 2, 9$). Data shown were collected under field-cooled (FC) conditions. The line over the powder data is a fit to the Curie–Weiss law. Powder samples were measured at an external field $H = 0.5$ kG and the PDMS composites at $H = 1$ kG. In all cases 3.5% weight perovskite was incorporated in the polymer matrix.

the particular morphology of the perovskite crystallites) the fraction of uncorrelated “surface” spins in dispersed samples is increased as compared to “bulk” spins. Such surface moments, lacking coherent nearest-neighbor superexchange interactions, lead to disordered spin configurations that give rise to a reduced average moment magnitude. However, the overall temperature dependence of the high-temperature spin susceptibility is very similar in all cases. The broad maximum of the $\chi(T)$ in both bulk and composite samples around ~ 60 – 70 K is indicative of the presence of antiferromagnetic correlations in these low-dimensional magnetic systems. The temperature dependence of the magnetic moment in the magnetically ordered phase ($T < T_N$) is also worthy of further discussion. The canted spin component of the antiferromagnetically coupled Mn^{2+} moments gives rise to a weak ferromagnetic behavior below T_N . This is evident in bulk as well as in composite samples as a sharp upturn in the susceptibility and a moderate deviation between ZFC and FC measurements. The behavior was attributed before to the antisymmetric Dzyaloshinsky–Moriya exchange interaction originating from the tilting of the MnCl_6 octahedral units inside the layers.^{9,10} We believe that the difference in the way the weak ferromagnetic moment develops lays on the inhomogeneous microstructure met in the composites. The enhanced surface areas and pronounced structural defects of the inorganic particles produce a certain degree of spin disorder (due to “broken” exchange bonds at the nearest-neighbor Mn-lattice sites), which in turn gives rise to a “distribution” of Néel temperatures and exchange constants.

In the composites the large diamagnetic contributions of the polymeric molecular chains to the paramagnetic spin susceptibility lead to a deviation of the $\chi(T)$ from the Curie–Weiss behavior, $(C/(T - \theta))$, an effect that prevented us from extracting a value for the magnitude of the effective magnetic moment in the paramagnetic T -range. For the bulk powder samples, we corrected the molar susceptibility for the diamagnetism of the constituent atoms and the alkylammonium chains (estimates based on the procedure developed by Pascal resulted in $\chi_{\text{diamagnetic}}^{\text{EA}} \sim -180 \times 10^{-6}$ emu/mol and $\chi_{\text{diamagnetic}}^{\text{NOA}} \sim -340 \times 10^{-6}$ emu/mol). Then we ex-

(17) van Amstel, W. D.; de Jongh, L. J. *Solid State Commun.* **1972**, *11*, 1423.

(18) de Jongh, L. J. *Magnetic Properties of Layered Transition Metal Compounds*; Kluwer Academic Publishers: Dordrecht, 1986.

(19) Kodama, R. H. *J. Magn. Mater.* **1999**, *200*, 359.

tracted an average $\langle\mu_{\text{eff}}\rangle(\cong(8C)^{1/2})\sim 6.6(4)\mu_{\text{B}}$ ($110\leq T\leq 300\text{ K}$), that within the experimental errors approaches the theoretically expected, $\sim 5.92\mu_{\text{B}}$, for a high-spin, $S=5/2$, Mn^{2+} state. Furthermore, Curie–Weiss fitting of the $\chi(T)$ data, for powdered perovskites with varying organocation chain length ($n=2, 9$), allowed a large negative paramagnetic Curie temperature, $\langle\theta\rangle\sim -130(5)\text{ K}$, that postulates to growing antiferromagnetic correlations already at elevated temperatures.

b. Microscopic Electronic Response by EPR. Comparing the behavior of the bulk O–I perovskite powders to the EPR response arising from the lower dimensional inorganic layered microstructure afforded in the composite system, useful conclusions are drawn on the type of interactions met in anisotropic Heisenberg magnets. One can determine the temperature dependence of the paramagnetic, spin-only susceptibility by measuring the intensity of the EPR signal. This has the advantage of being free from “parasitic” diamagnetic susceptibility signal arising from the organic constituents of the hybrid system. The purpose is to provide insight on the spin dynamics in the particular 2D topology achieved by increasing the organocation (alkylammonium) chain length.

Static Properties. The calibrated EPR signal intensity, at room temperature, for dispersed $(\text{EA})_2\text{MnCl}_4$ and $(\text{NOA})_2\text{MnCl}_4$ in PDMS corresponds to $\mu_{\text{eff}}\cong 4.0\mu_{\text{B}}$ and $\mu_{\text{eff}}\cong 4.4\mu_{\text{B}}$, respectively. The paramagnetic effective magnetic moment appears reduced compared to values obtained in bulk powders, in agreement with the magnetization measurements described above. Also the temperature dependence of the EPR signal intensity, observed in bulk samples, does not deviate from that reported in previously published results.²⁰ The spin susceptibility, given by the intensity of the EPR signal, is characterized by a broad maximum around $\sim 70\text{ K}$ and is rather similar for all the samples at temperatures $T > 60\text{ K}$ (Figure 4). In a 2D square-lattice Heisenberg model the spin susceptibility at high temperatures can be analyzed by the expression²¹

$$\chi = \frac{\beta g^2}{3} \left(\frac{1 + L(-\beta J')}{1 - L(-\beta J')} \right)^2 \quad (1)$$

where the only free parameter is the intralayer exchange coupling constant J , given by $J' = JS(S+1)$, with $S=5/2$ for Mn^{2+} ions. Here $L(x)$ is the Langevin function, g the Landé factor, $\beta = 1/kT$, and k the Boltzmann constant. Unconstrained fit using eq 1 (taking into account only measurements between $60 < T < 300\text{ K}$) allows for an estimate of the magnitude of the average intralayer exchange coupling constant, $J \sim -7.5\text{ K}$, for both bulk and PDMS-based samples (Table 2). On the basis of these measurements we can conclude, that the intralayer exchange does not vary substantially from sample to sample; i.e., it does not change considerably either with n nor with the dispersion in the PDMS matrix and the composite formation.

Interestingly, we find an EPR signal even in the magnetically ordered phase. This response, at $T < T_{\text{N}}$, is not

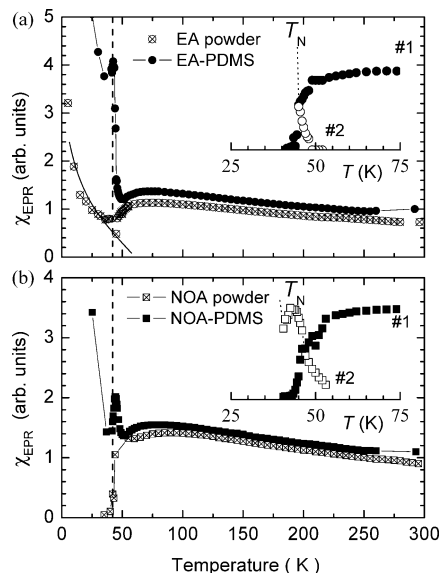


Figure 4. Temperature dependence of the total EPR spin susceptibility in EA and NOA, powder and composite samples. In both (a) and (b) “crossed” symbols represent measurements of bulk powder, while “solid” symbols are due to PDMS-based samples. The line over the EA data below T_{N} indicates the Curie-like contribution that survives in the EPR spectra of bulk powders. Insets in (a) and (b) show the temperature dependence of the individual components arising from the deconvolution of the EPR spectra in the composites into two Lorentzian lines. The “high-temperature” component (1) vanishes at T_{N} , while the “low-temperature” component (2) appears to develop already just above T_{N} . The latter completely dominates the spectrum at lower temperatures.

attributed to an antiferromagnetic resonance type signal. While it is possible that this is due to some paramagnetic impurities, its intensity quantitatively differs in bulk and composite samples, making its origin worthy to be investigated further. For instance, in bulk $(\text{NOA})_2\text{MnCl}_4$ sample the EPR susceptibility nearly vanishes below $T_{\text{N}} \cong 41 \pm 2\text{ K}$ and only at very low temperatures a very weak EPR line, with a Curie-like dependence, appears (Figure 4). On the other hand in PDMS-based samples one can notice the deviation of the EPR signal from a simple Lorentzian line shape already a few degrees kelvin above T_{N} . The difference in the line shape can be modeled as a superposition of two overlapping Lorentzians. Then one can notice that the “high-temperature” signal 1 disappears at T_{N} , while the “low-temperature” signal 2 increases strongly with decreasing temperature (inset, Figure 4). This approach then supports a “dual” nature for the EPR response in the vicinity of the Néel temperature. Taking into account the structural considerations discussed in Structure and Morphology of Composites, we envisage that the “low-temperature” signal is mainly due to the spins located at or near the many structural defects, including the surface and stacking faults, of the composites.

Low-Energy Magnetic Excitations. Furthermore, the dynamic spin correlation function in the paramagnetic phase and the magnetic anisotropy are probed by the temperature dependence of the EPR line width. To this extent, some marked differences between samples composed of short and long $\text{C}_n\text{H}_{2n+1}\text{NH}_3^+$ groups are observed even at room temperature. In $(\text{EA})_2\text{MnCl}_4$ -based ($n=2$) samples, the peak-to-peak EPR line width at 300 K is comparable, namely, $\Delta H_{\text{pp}} = 23.8$ and 23.5 G in bulk and dispersed samples,

(20) Benner, H. *Phys. Rev. B* **1978**, *18*, 319.

(21) Curely, J.; Rouch, J. *Physica B* **1998**, *254*, 298.

Table 2. Intralayer Exchange Coupling Constant, J , and the Néel Ordering Temperature, T_N , Extracted from the Calibrated EPR Signal Intensity^a

compound	bulk parent perovskite			polymer nanocomposite		
	J/K	T_N/K	E_S/K	J/K	T_N/K	E_S/K
(EA) ₂ MnCl ₄	-7.5(2)	41(2)	673(20)	-7.6(2)	42(2)	636(20)
(NOA) ₂ MnCl ₄	-7.8(3)	43(2)	570(30)	-7.7(1)	43.5(2.0)	528(20)

^a The activated behavior of the line width, eq 2, allows the magnitude of the pinned soliton energy, E_S , to be estimated.

respectively. On the contrary, the difference is large in (NOA)₂MnCl₄ ($n = 9$) samples. The room-temperature peak-to-peak EPR line width in bulk powder is $\Delta H_{pp} = 31.1$ G, while it is $\Delta H_{pp} = 23.8$ G in the composite. Such an increase in the EPR line width of bulk samples may be attributed to the enhanced magnetic anisotropy in (NOA)₂MnCl₄. This has been recently suggested to be the cause for the raise in the magnitude of T_N with increasing n .²² On the other hand, in PDMS-based (NOA)₂MnCl₄ sample the room-temperature line width is almost the same as in {(EA)₂MnCl₄-PDMS} composite. We believe that the interaction between the organophilic alkylammonium chain with the PDMS plays a major role here.

Early detailed investigations²³ on the (C_{*n*}H_{2*n*+1}NH₃)₂MnCl₄ compounds have shown that coupling of the dynamical motion of the alkylammonium groups to the tilting pattern of the MnCl₆ octahedra gives rise to order-disorder transitions (T_{O-D} : followed by change in the lattice symmetry) in the bulk perovskite samples, which apparently shift from $T_{O-D} \leq 200$ K, in $n \leq 3$, toward room temperature¹⁰ with further increase in n . XRD analysis has shown (in X-ray Diffraction Considerations) that in the {(NOA)₂MnCl₄-PDMS} sample the interlayer distance of the perovskite increases by at least 2 Å during the composite formation. This suggests partial intercalation of the polymer chains between the layered structure that in turn inhibit the reorientational dynamics of C_{*n*}H_{2*n*+1}NH₃⁺ chains through steric interactions. The structure then appears “stiffer”, i.e., attains a relatively stronger interlayer bonding and in this respect even the {(NOA)₂MnCl₄-PDMS} sample becomes “similar”, in terms of layer coupling, to (EA)₂MnCl₄-based materials. This behavior is reflected in the temperature dependence of the peak-to-peak EPR line width for the NOA composite, with the subsequent lowering of the order-disorder transition (as marked by important changes in the slope of the otherwise linear $\Delta H_{pp}(T)$ curves) from the ~ 290 K value, observed in the bulk powder NOA material, to $T_{O-D} \sim 200$ K.²⁴

Below 70 K in all four samples the EPR line width starts to increase substantially. This low-temperature region is a fluctuation region where the spin excitations determine the EPR line width. Both static solitons coupled to magnons and magnons themselves were suggested before as the main source of broadening between 70 K and $\sim T_N$.²⁵ In this case the temperature dependence of the EPR line width should

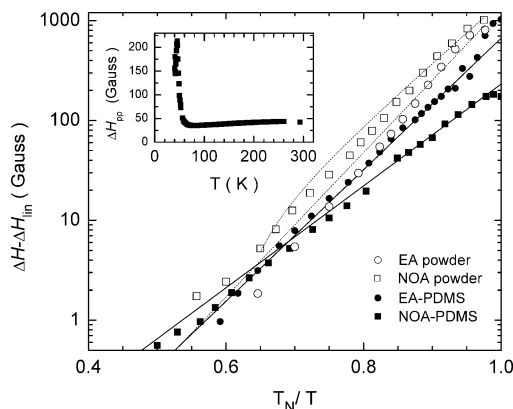


Figure 5. Temperature dependence of the EPR line width, $\Delta H - \Delta H_{lin}$, just above the Néel temperature, having subtracted the high-temperature linear contribution. The solid lines represent the fit to the eq 2. Inset: displays the characteristic temperature evolution of the EPR line width for one of the composites, i.e., the {(NOA)₂MnCl₄-PDMS}, before the subtraction of the linear term.

follow approximately an Arrhenius law,²⁶ namely, $\Delta H \propto \exp(E_S/T)$. Here $E_S = 4\pi JS^2$ is the soliton energy. More precisely the EPR line width²⁷ should change according to the following relation:

$$\Delta H \sim \frac{T}{\chi_{\perp}} \left[\frac{4^3 S}{2\sqrt{2}} \left(\frac{T}{JS^2} \right)^{3/2} + \sqrt{\frac{2\pi JS^2}{T}} \left(\frac{T}{JS^2} \right)^4 \xi \right] \xi^2 \quad (2)$$

where $\chi_{\perp} = (1/8)J$ and $S = 5/2$. The main temperature dependence comes from the temperature dependence of the correlation length:²⁸

$$\xi = \frac{1}{8e^{\pi/2}\sqrt{2}} \exp\left(\frac{E_S}{2T}\right) \quad (3)$$

After subtracting the high-temperature linear line width, the remaining contribution to the line shape indeed follows the above-mentioned activated type of behavior and is nicely fitted to eq 2. The least-squares fitted curve(s) together with a low-temperature data are shown in Figure 5. The extracted parameters are compiled in Table 2. For example, the derived value of the soliton energy for the bulk (EA)₂MnCl₄ powder is $E_S \cong 673$ K. The latter is in fairly good agreement with the magnitude of E_S determined by utilizing equation $E_S = 4\pi JS^2$ and J values extracted from the temperature-dependent EPR susceptibility. We notice though that the extracted soliton energy is somehow smaller in bulk (NOA)₂MnCl₄ sample. The decrease is even more dramatic when PDMS-based samples are compared (Table 2). The observed reduction of E_S resembles the effect of impurity centers to

(22) Lee, K. W.; Lee, C. H.; Lee, C. E.; Kang, J. K. *Phys. Rev. B* **2000**, *62*, 95.

(23) Heger, G.; Mullen, D.; Knorr, K. *Phys. Status Solidi A* **1975**, *31*, 455. Heger, G.; Mullen, D.; Knorr, K. *Phys. Status Solidi A* **1976**, *35*, 627; Kind, R. *Ferroelectrics* **1980**, *24*, 81.

(24) See Supporting Information.

(25) Zaspel, C. E.; Grigoreit, T. E.; Drumheller, J. E. *Phys. Rev. Lett.* **1995**, *74*, 4539.

(26) Waldner, F. *J. Magn. Magn. Mater.* **1983**, *31-34*, 1203. Waldner, F. *J. Magn. Magn. Mater.* **1983**, *54-57*, 873.

(27) Zaspel, C. E.; Drumheller, J. E. *Int. J. Mod. Phys. B* **1996**, *10*, 3648.

(28) Takashi, M. *Phys. Rev. B* **1989**, *40*, 2494.

pin-down solitons in two-dimensional Heisenberg antiferromagnets.²⁹ For instance, from the relative diminution of E_S in $\{(EA)_2MnCl_4-PDMS\}$ and comparison to earlier theoretical calculations²⁹ we can estimate that $\sim 0.5\%$ nonmagnetic impurities can be present in the perovskite lattice. Assuming this occurs in the longitudinal dimension of an extended layer stack we calculate an ~ 140 -nm particle size. This is comparable to the values estimated from the TEM measurements. Therefore, wherever the PDMS chains tend to enter into the layer stacks, it is a cause for defect structure formation that can influence the low-temperature spin dynamics.

The EPR data appear to correlate well with the structural and morphological observations involving the composite formation. Though finite particle size effects appear not to have a significant result on the bulk magnetic properties (e.g., magnitude of T_N and nature of the transition), local scale imperfections in the morphology “soften” the low-energy magnetic excitations (pinned solitons). Also the increased surface-to-volume ratio in dispersed samples is clearly reflected in the reduction of the effective moment measured by the intensity of the EPR signal.

Concluding Remarks

We have prepared polymer composites based on $(R_n-NH_3^+)_2MnCl_4$ ($R_n = C_nH_{2n+1}$; $n = 2, 9$) layered hybrid perovskites. Their magnetic properties were measured and compared to the corresponding behavior of bulk powder samples while the influence of the organocation chain length was also addressed. The interaction between the PDMS matrix and the alkylammonium chains depends on the alkyl group chain length and is reflected in the composite's morphological characteristics. We find disordered but also mutually oriented layer groupings for $\{(EA)_2MnCl_4-PDMS\}$ and $\{(NOA)_2MnCl_4-PDMS\}$ composites, respectively, which establish an inhomogeneous microstructure. While the $(EA)_2MnCl_4$ crystallites maintain their gallery heights in their composites, a pronounced layer delamination is seen at the interfacial regions with the polymer. On the other hand,

partial polymer intercalation is witnessed at the interfaces of $(NOA)_2MnCl_4-PDMS$, giving rise to increased structural defects, including surface and stacking faults. The interpenetration of the PDMS polymer chains and alkylammonium groups in the interlamellar NOA-based perovskitic space results in relatively stronger interlayer bonding, inhibiting the dynamics of the alkylammonium part of the perovskitic structure. We find that the major characteristics of the magnetism, pertaining to a 2D antiferromagnetic Heisenberg behavior, explored in bulk powders survive also in the composites. However, the finite size effects enter into the systems through numerous structural irregularities related to regions of partial PDMS intercalation and the enhanced surface area in addition to defects created during the composite formation. In turn these modifications of the local microstructure can suppress the degree of long-range magnetic order while in confined geometries act as nonmagnetic pinning centers for the low-temperature solitonic excitations. Therefore the dynamical magnetic properties of the dispersed samples seem to follow some of the changes in the particle morphology. Further investigations on longer chain perovskitic compounds and utilization of alternative conditions for the polymer composite formation could eventually afford nanoscale $MnCl_4^{2-}$ -based layers of enhanced functionality to that in analogous silicate nanocomposites.

Acknowledgment. The present work was supported by the Marie Curie Fellowship program of the European Commission under Contract No. HPMD-CT-2000-00050 (E.W.). Partial financial support through a “Joint Research & Technology Programme” of the General Secretariat for Research & Technology (Greece) with the Ministry of Education, Science and Sport of the Republic of Slovenia is acknowledged. We thank M.A. Green and D. Arnold (Royal Institution of Great Britain) for help with the SQUID measurements and S.H. Anastasiadis for fruitful discussions on polymer-clay nanocomposites.

Supporting Information Available: Extensive figures on the temperature dependence of the EPR line width in bulk EA and NOA powders as well as in PDMS composite samples. Discussion of how the changes in the line width are assigned to the order–disorder structural transitions in the perovskites. This material is available free of charge via the Internet at <http://pubs.acs.org>.

CM048744P

(29) Subbaraman, K.; Zaspel, C. E.; Drumheller, V. *Phys. Rev. Lett.* **1998**, *80*, 2201.